Error analysis and applications of a general QM/MM approach

Yi Zhao [a,b,*], Chongyu Wang [b], Qing Peng [b], Gang Lu [b]

[a] Department of Physics, Tsinghua University, Beijing 100084, PR China
[b] Department of Physics and Astronomy, California State University Northridge, Northridge, CA 91330-8268, USA

ARTICLE INFO

ABSTRACT

Combing computational efficiency and accuracy, quantum mechanic/molecular mechanic (QM/MM) methods are promising for understanding and predicting materials properties at atomic scales. We present a general QM/MM method that can be implemented in a variety of QM and MM combinations; we focus on a tight-binding and a plane-wave pseudopotential methods for the QM part and the Stillinger–Weber and EAM potentials for the MM part. The QM/MM coupling errors are analyzed. It is found that a sufficient size of the coupling region and the buffer zone is crucial in minimizing the coupling errors. On the other hand, the size of the weighting zone turns out to be less important. The QM/MM method is applied to model the dynamical propagation of Si cracks with different orientations and under different mode I loadings. The QM/MM method is found to correctly reproduce the brittle fracture of Si, whereas the SW potential fails to do the same. The QM/MM method is also used to study the ductile fracture in Au and compared to the EAM potential. Finally, the QM/MM method is applied study the vacancy diffusion in a Cu grain boundary. The QM/MM results compare very well to the previous EAM results.

Published by Elsevier B.V.

1. Introduction

Multiscale modeling of materials has attracted a great deal of interest recently because real materials usually exhibit multiphysics phenomena that at one scale require a very accurate and computationally expensive description, and at another scale, a coarser description is often satisfactory and, in fact, necessary to avoid prohibitively large computations [1]. For example, quantum mechanics (QM) is required for a proper treatment of bond-breaking, bond forming, charge transfer, electron excitation, and magnetism, etc., in materials. However, due to the demanding computational cost, the application of QM has to be limited to relatively small systems consisting of up to a few hundreds of atoms. On the other hand, atomistic simulations based on empirical interatomic potentials are capable of describing small-amplitude vibrations and torsions, elastic deformation and electrostatic interactions, etc., in many materials and biological systems [2,3]. Termed as molecular mechanics (MM) methods, these empirical atomistic approaches can treat millions of atoms, and with simpler potentials, even billions of atoms [4]. Therefore, as a multiscale modeling approach, the QM/MM coupling [5–7] that combines the accuracy of QM with the low computational demand of MM

represents an attractive strategy to deal with large material systems with desired accuracy.

In a typical QM/MM approach a system is partitioned into two spacial regions: region I containing lattice defects and/or chemically active domain, where QM description is mandatory; and region II – the rest of the system which can be described by empirical MM methods. The schematic partition of QM/MM is shown in Fig. 1a. In general, the total energy of a QM/MM system can be written as:

$$E_T = E^{QM}[I] + E^{MM}[II] + E^{int}[I, II], \qquad (1)$$

the three terms on the right hand side are: QM energy of region I, MM energy of region II and the interaction energy between regions I and II. The crux of a QM/MM method lies in its handling of $E^{int}[I, II]$, which can be treated at different levels of approximation. Depending on the formulation of $E^{int}[I, II]$, QM/MM methods can be classified into two broad categories: mechanical embedding (ME) and electronic embedding (EE). In ME, $E^{int}[I, II]$ is formulated at the MM level and the regions I and II are coupled mechanically. On the other hand, in EE $E^{int}[I, II]$ is treated quantum mechanically [8–10] and the two regions are coupled electronically. In general, EE is formulated based on a more rigorous theoretical footing comparing to ME, and is thus more accurate [8–16]. On the other hand, EE is more complex and often computationally more expensive to ME.

In this paper, we focus on a general QM/MM approach that is based on ME. Although the similar QM/MM methods have been
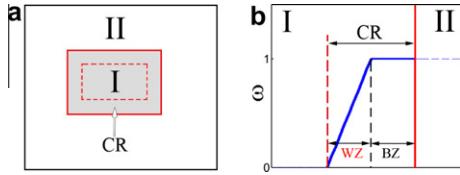
Fig. 1. (a) Schematic partition of the QM/MM system into region I (in gray) and region II. The region I is further subdivided into an inner region (dashed box) and a coupling region (CR). (b) The form of the weighting function ω in relation to the weighted zone (WZ) and the buffer zone (BZ).

discussed in literature [17–19], detailed analysis of coupling error is of crucial importance. As it was reported previously [5,20] and will be shown in this paper, significant coupling errors could arise that would render simulation results worthless if certain computational parameters are not chosen judiciously. Finally we apply the QM/MM method to address a number of challenging problems that involve extended defects in both Si and metallic systems.

2. Methodology

In the present QM/MM approach, the interaction energy $E^{\text{int}}[\text{I,II}]$ is determined by an MM method, i.e.

$$E^{\text{int}}[\text{I,II}] = E^{\text{MM}}[\text{I,II}] - E^{\text{MM}}[\text{I}] - E^{\text{MM}}[\text{II}]. \qquad (2)$$

Here $E^{\text{MM}}[\text{I,II}]$, $E^{\text{MM}}[\text{I}]$ and $E^{\text{MM}}[\text{II}]$ represent the energy for the entire system, regions I and II, respectively using the same MM method. Therefore, the total energy of the system becomes

$$E_{\text{T}} = E^{\text{QM}}[\text{I}] + E^{\text{MM}}[\text{I,II}] - E^{\text{MM}}[\text{I}], \qquad (3)$$

and the atomic forces on the ith atom can be written as

$$-\mathbf{F}_i = \frac{\partial E^{\text{QM}}[\text{I}]}{\partial \mathbf{r}_i} + \frac{\partial E^{\text{MM}}[\text{I,II}]}{\partial \mathbf{r}_i} - \frac{\partial E^{\text{MM}}[\text{I}]}{\partial \mathbf{r}_i}, \qquad (4)$$

where $\mathbf{r}_i$ denotes the coordinate of the ith atom. This QM/MM method can be interpreted as applying a QM correction to the MM description of region I since MM is considered not accurate enough for region I [11]. A major practical advantage of this approach is that, if region I contains many different atomic species while region II contains only one atomic type, there is no need to have a classical potential for each species and their interactions. This results from the fact that if the various species of atoms are well within region I, then the energy contributions of these atoms cancel out in the total energy calculation (the last two terms in Eq. (3)). Thus, this coupling approach is particularly useful in dealing with impurities, which is an exceedingly difficult task for classical MM simulations.

In this paper, we focus on the calculation of atomic force and attempt to minimize the coupling errors in the force calculations. As shown in Fig. 1a, the computational model is divided into regions I and II as indicated by the solid boxes. In addition, the region I is subdivided into an inner region (within the dashed box) and a so-called coupling region (CR). For the atoms in the inner region, the atomic force is calculated according to Eq. (4). In practice, since these atoms are well inside region I, only the first term $\partial E^{\text{QM}}[\text{I}]/\partial \mathbf{r}_i$ survives. In the coupling region, however, the atomic force, $\mathbf{F}_i^{\text{QM/MM}}$ is calculated as:

$$\mathbf{F}_i^{\text{QM/MM}} = \omega \mathbf{F}_i^{\text{MM}}[\text{I,II}] + (1 - \omega)\mathbf{F}_i, \qquad (5)$$

where $\mathbf{F}_i^{\text{MM}}[\text{I,II}] = -\partial E_{\text{MM}}[\text{I+II}]/\partial \mathbf{r}_i$, and $\mathbf{F}_i$ is given in Eq. (4). The weighting function ω is defined in the coupling region only and the form of ω is shown in Fig. 1b. Furthermore, the coupling region in general consists of two parts: (1) a "buffer zone" (BZ) in which $\omega = 1$ and (2) a linearly weighted zone (WZ) which smoothes

the mixture of QM and MM forces. The purpose of the buffer zone is the same as that of the "boundary region" introduced by Liu et al. [17]. Namely, it can reduce the fictitious surface effect of the cluster calculation of region I. In specific, because the first and the third term in Eq. (4) does not cancel for the surface atoms in general, the discrepancy is a significant source of the coupling errors. By introducing the BZ, this error is greatly reduced. Although the BZ atoms are included in the QM calculations, i.e., they are region I atoms, the force on these atoms is actually determined by the MM calculation of the entire system – the fictitious surface effect is thus removed.

For the atoms in the coupling region, the force expression in Eq. (5) is no longer the derivative of the energy in Eq. (4). This inconsistency could lead to problems in atomic relaxation if a gradient-based minimization algorithm is used. To remedy for this inconsistency, one can define a so-called correction force for the atoms in CR as:

$$\mathbf{F}_i^{\text{corr}} = \mathbf{F}_i^{\text{QM/MM}} - \mathbf{F}_i = \omega\left(\mathbf{F}_i^{\text{MM}}[\text{I}] - \mathbf{F}_i^{\text{QM}}[\text{I}]\right), \qquad (6)$$

where $\mathbf{F}_i^{\text{QM}}[\text{I}] = -\partial E_{\text{QM}}[\text{I}]/\partial \mathbf{r}_i$ is the QM force in region I. The work done by the correction forces is thus

$$W_{\text{corr}} = \sum_{i \in CR} \int \mathbf{F}_i^{\text{corr}} \cdot d\mathbf{r}_i. \qquad (7)$$

Here $d\mathbf{r}_i$ and $\mathbf{F}_i^{\text{corr}}$ represent the displacement and correction force on atom i in CR during each relaxation step; the integration is over the entire relaxation trajectory. Therefore the corrected total energy E_{T}' is written as

$$E_{\text{T}}' = E_{\text{T}} + W_{\text{corr}}, \qquad (8)$$

where E_{T} is defined in Eq. (3). Note that E_{T}' is the actual energy being minimized using the gradient-based schemes and represents the appropriate total energy of the system.

In this paper we have used the NRL tight-binding (TB) model for region I in addition to the plane-wave method. The NRL-TB approach has been extensively calibrated and reproduces well the band structure and bulk properties [21–24] from more accurate density functional theory (DFT) results. The elements of the nonorthogonal TB Hamiltonian and overlap matrix are parameterized as a function of the atomic structure under the two-center approximation [25]. For region II, we have used the Stillinger–Weber potential (SW) of Si [26] and the Johnson EAM potentials for Au and Cu [27]. The following error analysis is carried out to examine the general QM/MM scheme with TB/SW coupling as an example.

3. Error analysis

Ideally, a successful QM/MM scheme should ensure that the QM/MM interface be transparent and not introduce fictitious discontinuities. However inconsistencies between QM and MM methods do exist and the discontinuities could hardly be eliminated. Therefore, an error analysis of QM/MM methods is important, and particularly, the discontinuities across the interface should be closely examined. In practice, one can estimate the coupling errors by calculating the displacement from the equilibrium atomic position of a known structure, such as a perfect lattice. The magnitude of the displacement thus quantifies the coupling errors. The requirement of the interfacial transparency is often more rigorous in a molecular dynamics (MD) simulation than in a static relaxation. For MD, one has to insist that the same thermal conductivity be maintained across the interface so that the lattice vibrations are not impinged or reflected in a non-physical way.

First, the QM/MM scheme is tested in static atomic relaxations. The system is a Au thin film with a dimension of 4.06 Å $\times$ 4.06 Å $\times$ 160 Å in X, Y and Z direction, respectively. The periodical boundary
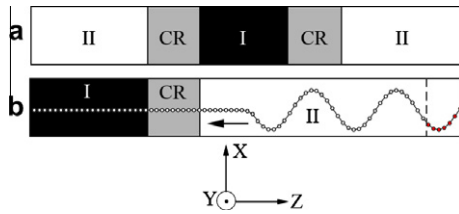
Fig. 2. Schematic partition of the computational model for error analysis. (a) For static relaxation and (b) for MD simulation. The atoms are shown in circles. The lattice vibrations are introduced from the right end of the model, represented by the red circles. (For interpretation of the references to colour in this figure legend, the reader is referred to the web version of this article.)

conditions (PBC) are applied in X and Y directions and an open boundary condition is applied in Z direction. The TB region with a width of 30 Å is sandwiched between two EAM regions in the middle of the system as shown in Fig. 2a. The EAM potential is scaled to match the lattice constant and bulk modulus of the corresponding TB values [8,9]. The simulations are carried out with different sizes of CR and WZ. The atomic displacement from the ideal equilibrium position, considered as the coupling error is show in Fig. 3. It is found that the displacement or the coupling error is significant for a small size of CR and WZ, which would render the simulation results worthless for a more complicated system. The error reduces considerably as the size of CR increases. On the other hand, the size of WZ seems to play a minor role. In other words, the error correction is primarily achieved by the introduction of the buffer zone; the mixture of QM and MM forces does not play an important role in cutting down the errors.

In Fig. 4, we present the variations of the energetics during the static relaxation. It is observed that the corrected total energy E_T'
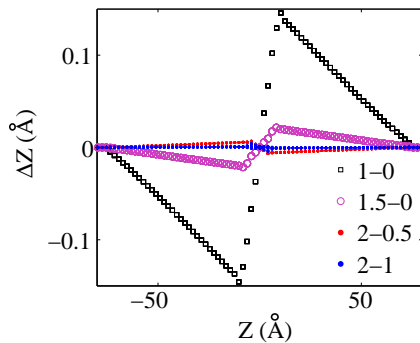
Fig. 3. Atomic displacement as a function of Z coordinate for different choices of CR and WZ size. The first and second number in legends refers to the size of CR and WZ in terms of the lattice constant a_0.
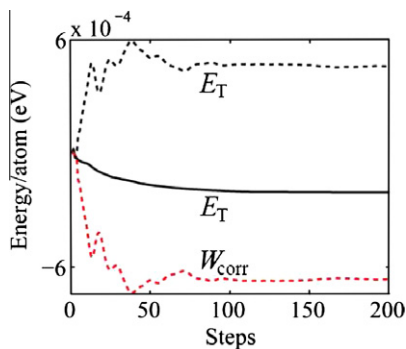
Fig. 4. The energy variation in the static relaxation as a function of the iteration step. The energy is set to zero at the initial step. E_T' and E_T are the total energy with and without the correction respectively; W_{corr} is the correction energy.
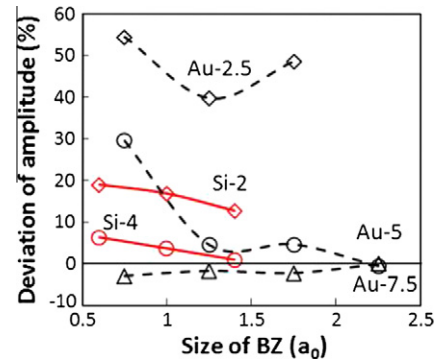
Fig. 5. The maximum deviation of the vibrational amplitude measured as a function of the buffer zone size. For example, the legend "Si-2" refers to the system of Si and the width of CR is $2a_0$.

decreases monotonically in the relaxation while the original energy fluctuates especially at the initial stage of the relaxation. Therefore, using the corrected total energy, one can employ the gradient-based minimization algorithms such as the conjugated gradient methods in static relaxations that are often more efficient than the force-based algorithms.

The second test is performed to examine the transparency of the QM/MM interface to lattice vibrations. Si and Au thin films are simulated with the computational setup similar to the static relaxation except that the region I is placed at the left side of the system with the coupling interface placed at 50 Å from the left end. The schematic partition of the computational model is shown in Fig 2b. Both longitudinal and transverse lattice vibrations are introduced from the right end of the model and propagate towards the region I. The amplitude of the waves is 0.3 Å and the driving frequency is 3×10^{12} Hz. After the vibrational waves propagate into the region I, the reflected waves, if any, will overlap with the incident waves and result in a change of wave profile. Thus the interfacial transparency may be evaluated by the change of the wave amplitude. The results for both Si and Au thin films are summarized in Fig. 5. Once again, significant errors exist for smaller sizes of CR and BZ. The change of the wave amplitude is measured as a function of the CR and BZ size. It is shown that the width of CR is again the critical factor affecting the interfacial transparency. This width seems to more important for Au comparing to Si, perhaps due to the delocalized electronic states and longer-range of the atomic interactions in Au. In addition, it is found that the required CR size is larger for the longitudinal wave than for the transverse wave due to the fact that the longitudinal vibrations are in the same direction of the coupling errors. Finally, the coupling errors decrease monotonically as a function of the BZ size in Si; but no such behavior is observed in Au.

We find that the CR size of 7 Å and 10 Å is sufficient to converge the results for Si and Au respectively; the critical sizes are close to the corresponding TB cut-off parameters for Si and Au [23,24]. For the plane-wave pseudopotential methods (such as VASP), we find the critical CR size to be 2 Å for a good convergence. The much smaller critical size is due to the screening effect that is well captured by these more accurate DFT methods.

4. Applications

4.1. MD simulations of si fracture

Brittle fracture of Silicon has been widely studied both theoretically and experimentally owing to the technological importance of Si. It was observed experimentally that Si was very brittle at room

temperature, with sharp crack tips propagating along the {111} and {110} planes leaving behind flat surfaces [28]. However, MD simulations based on empirical potentials failed to predict the brittle fracture of Si [21,29,30,18,19,31]. Since treating the entire crack quantum mechanically is not realistic, we resort to the QM/MM method which is ideal for modeling fracture.

Four types of mode I cracks under different loading conditions have been simulated in the paper: {110}⟨001⟩, {110}⟨110⟩, {111}⟨110⟩ and {111}⟨112⟩. The crack with the {110} cleavage plane propagating towards ⟨001⟩ direction is denoted as {110}⟨001⟩ hereafter. A plane strain field [34,35] of a straight mode I crack is introduced to generate the initial crack structure. The displacement field of the atoms at the edges of the simulation box remains fixed during the simulations. The simulation cell measures 500 Å along the propagating direction (horizontal), 275 Å perpendicular to the cleavage plane (vertical), and a period along the crack front line (normal to the page) in which the PBC is applied. The periodic distance is 3.84, 5.43, 6.65 and 3.84 Å for the {110}⟨001⟩, {110}⟨110⟩, {111}⟨110⟩ and {111}⟨112⟩ cracks, respectively. The width of CR and BZ is 15 Å and 5 Å respectively. The number of atoms in the systems ranges approximately from 23,000 to 45,000 for different cracks, and the number of atoms in region I ranges approximately from 220 to 380 depending on the orientation, loading and instantaneous structure in the MD simulation. The critical loading of the cracks is given in terms of the energy release rate, following the Griffith criterion G_c, which is 3.4 and 2.7 J/m^2 for {110} and {111} cracks respectively. The leap-frog Verlet algorithm is used in the MD simulations, with the time step of 3 fs and the temperature at 300 K under the Berendson thermostat [36]. The partition of the QM/MM domains is updated in every 20 MD steps.

It is found for the {110}⟨001⟩ crack both the QM/MM and the stand-alone SW MD simulations predict that the crack will change to {111}⟨112⟩ direction, which agrees with both experimental and theoretical reports [32,33]. However for the other three orientations the QM/MM and SW methods give drastically different results. The results of the crack propagation speed are summarized in Table 1 and the comparison of the atomic structures is shown in Fig. 6. The QM/MM simulations yield flat crack surfaces which agrees with experimental observations of the brittle fracture. The {110} crack starts to propagate under 1.0 G_c at a speed of 600 m/s, and the speed increases with the loading. For the {111}⟨112⟩ crack, at loadings of 1.5 G_c and 2.5 G_c the propagation speed is 1500 m/s and 3000 m/s respectively, which is in good agreement with experimental values [31]. In a strong contrast to the QM/MM results, the SW potential predicts no propagation of the {111}⟨112⟩ crack even under the maximum loading of 2.5 G_c applied in the simulations. For the two other cracks, the propagation speeds are much lower. In particular, the SW MD predicts that the crack tip would blunt in all three cases, which are contradictory to the brittle nature of the cracks. The failure of reproducing brittle fracture in Si is the hallmark of the empirical MD simulations which cannot capture the bond-breaking correctly at the crack tip.

Table 1
Propagation speed of the cracks with different orientations and loadings. Upper rows are from the QM/MM calculations and the lower rows are from the SW potential. The unit of velocity is 10^3 m/s.

Load (G_c)	Method	1.0	1.5	2.5
{110}⟨110⟩	TB/SW	0.6	1.2	2.1
	SW	0.02	0.2	0.7
{111}⟨110⟩	TB/SW	0	1.7	3.1
	SW	0	0.05	0.8
{111}⟨112⟩	TB/SW	0	1.5	3.0
	SW	0	0	0
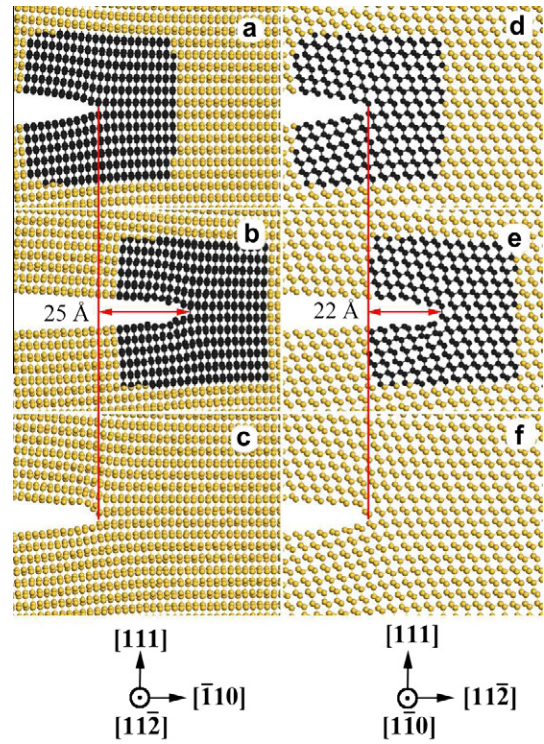
Fig. 6. Atomic structures of Si {111}⟨100⟩ (left column) and {111}⟨112⟩ (right column) cracks under a loading of 1.5 G_c. Upper row: the initial structures and the regions I and II atoms are in black and gold respectively; Middle row: after 1.5 ps by the QM/MM MD method; the arrow indicates the distance that the crack tip has travelled; Bottom row: after 1.5 ps by the SW MD method; the cracks do not propagate. (For interpretation of the references to colour in this figure legend, the reader is referred to the web version of this article.)

4.2. Static simulation of Au crack

The QM/MM method can also be applied to study ductile fracture in metals. As an example, we model the fracture of the {110}⟨111⟩ crack in Au under mode I loading at 0 K. The crack is generated by taking three semi-infinite {110} atomic layers away from a bulk Au and applying a prescribed displacement field as a function of the stress intensive factor (SIF) K_I following the solution of the anisotropic Linear Elastic Fracture Mechanics [37]. The dimensions of simulation model are 400 Å × 400 Å × 4.97 Å in [111], [110] and [112] directions, respectively. The PBC is applied along the crack front line [112] and the exterior boundaries are fixed. The region I is a disk with a radius of 20 Å centered at the crack tip and the width of the CR is 10 Å. There are approximately 320 atoms in region I and 46,196 atoms in the entire system. The TB method is coupled to EAM to carry out static relaxations. The structural optimization is performed with an iterative Broyden–Fletcher–Goldfarb–Shanno (BFGS) scheme [38] with a convergence criterion of 0.02 eV/Å in terms of atomic force for all atoms. The EAM potential is scaled to match the lattice constant and bulk modulus of the corresponding TB values. The load is applied to the fixed atoms at the exterior boundaries which corresponds to a certain SIF for the crack. The increment of SIF is 0.001 eV/Å$^{2.5}$ and 0.005 eV/Å$^{2.5}$ for the EAM and QM/MM calculations respectively. By the Griffith's criterion the minimum SIF for a crack propagation is $K_{IC} = \sqrt{2\gamma E} = 0.39$ eV/Å$^{2.5}$; here 2γ is twice the surface energy and E is the Young's modulus, whose TB values are 2.97 J/m^2 and 128 GPa respectively. Both the EAM method and the QM/MM (or TB/EAM) method predict a ductile fracture behavior in which dislocations are nucleated at the crack tip at a load much lower than K_{IC}. In specific, the QM/MM method predicts

that at a critical load of $K_I = 0.10$ eV/Å$^{2.5}$ a pair of edge dislocations are nucleated at the crack tip (as shown in Fig. 7) while the EAM predicts a higher critical SIF of 0.122 eV/Å$^{2.5}$. Increasing the load, the dislocations will move further away from the crack tip before more dislocations are nucleated.

4.3. Vacancy diffusion in Cu grain boundary

As the last example, we apply the QM/MM method to calculate the vacancy diffusion energy barrier in a Cu grain boundary (GB). A pseudopotential plane-wave method implemented in the VASP package [39] is used for the QM component. The projected augmentation wave method [40] under the Generalized Gradient Approximation [41] is used. The QM–VASP method is coupled to an EAM potential of Cu [27] to carry out the QM/MM calculations. The transition state and the corresponding diffusion energy barrier is determined based on the nudged elastic band (NEB) method [42]. The simulated system is a symmetric tilt $\Sigma5(\bar{2}10)[001]$ GB and measures 100 Å × 32.5 Å × 29.1 Å along $[\bar{2}10]$, $[120]$ and $[001]$ direction respectively. A fixed boundary condition is applied along the $[\bar{2}10]$ direction and PBC are applied to the $[120]$ and $[001]$ directions respectively. A vacancy is introduced at a lattice site adjacent to the GB plane labeled as "A" in Fig. 8 as the initial
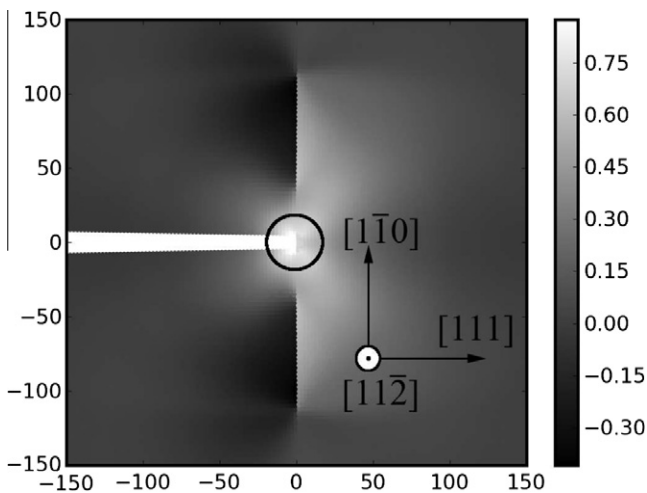
Fig. 7. Contour plot of the QM/MM displacement along the crack front line direction under the critical stress intensity for dislocation nucleation at $K_I = 0.10$ eV/Å$^{2.5}$. The region I is inside the circle. The unit of length is in Å.
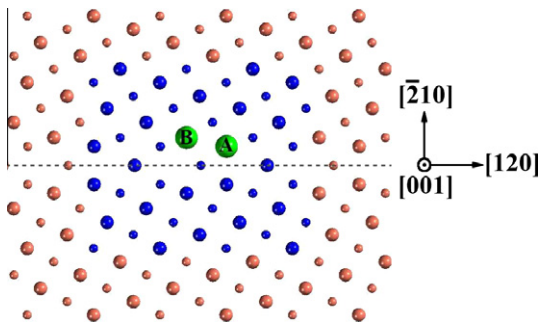
Fig. 8. Vacancy diffusion in Cu $\Sigma5(\bar{2}10)[001]$ GB. The atoms in regions I and II are represented by the blue and bronze spheres respectively. The GB plane is denoted by the dashed line. The larger and smaller spheres represent the two adjacent atomic planes in $[001]$ direction. The initial and final positions of the vacancy are shown in green and labeled as A and B respectively. (For interpretation of the references to colour in this figure legend, the reader is referred to the web version of this article.)
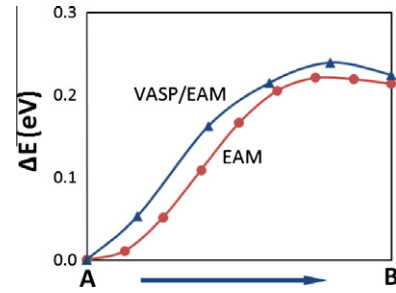
Fig. 9. Energy profiles of the vacancy diffusion from A to B in Fig. 8. Triangles and spheres denote the VASP/EAM and the stand-alone EAM results respectively.

position of the diffusing vacancy. The vacancy is then moved to an adjacent lattice site labeled as "B" in Fig. 8 as the final position. The QM region consists of 13 Å × 12 Å × 11 Å and it is placed at the center of the system to contain the entire diffusion path shown in Fig. 8. A coupling region of several Angstroms has been found to give converged results. There are 167 QM atoms and 8127 EAM atoms in the entire system. This particular diffusion path is chosen to compare with a previous EAM calculation by Sørensen et al. [43].

The diffusion energy profiles of the vacancy are shown in Fig. 9 using both the QM/MM (or VASP/EAM) and a stand-alone EAM methods. The EAM calculations predict a forward energy barrier of 0.221 eV for the vacancy diffusing from A to B and a backward energy barrier of 0.007 eV for the reverse process (B to A). The VASP/EAM calculation yields 0.239 eV and 0.015 eV for the forward and backward energy barriers, respectively. In comparison, the EAM calculations by Sørensen et al. [43] reported 0.231 eV and 0.002 eV for the forward and backward energy barriers, respectively. Note that the EAM potential used by Sørensen et al. is different from one we use in this calculation. Generally speaking, the three sets of calculations produce rather close results, with the VASP/EAM method giving slightly higher energy barriers. Therefore, we conclude that the QM/MM method works fine for this system and the EAM potentials for Cu are accurate for describing the vacancy diffusions in the GB.

5. Conclusion

We presented a general QM/MM method that can be implemented in a variety of QM and MM combinations. In this paper, we focus on the TB and the plane-wave pseudopotential methods for QM and the SW and EAM potentials for MM. The coupling errors are analyzed in details. It is found that a sufficient size of the coupling region and the buffer zone is crucial to obtain accurate results. On the other hand, the size of the weighting zone is found to be less important. These computational parameters are system dependent as expected. The QM/MM method is applied to three typical material simulations: MD, static relaxation and energy barrier calculations. In specific, we model the dynamical propagation of Si cracks with different orientations and under different mode I loadings. The QM/MM method can correctly reproduce the brittle behavior of Si fracture which the SW potential fails to do so. The QM/MM method predicts a crack propagation speed that is comparable to the experiment. The QM/MM method is also used to study the ductile fracture in Au and compared to the EAM results. It is found that the EAM overestimates the critical load for dislocation nucleation by 20%. Finally, the QM/MM method is applied to study the vacancy diffusion in a Cu grain boundary. The QM/MM results compare very well to the previous EAM results, which in turn validates both the reliability of the QM/MM method and the validity of the EAM potentials for describing Cu GB diffusions.

Acknowledgement

References

[1] G. Lu, E. Kaxiras, M. Rieth, W. Schommers, Handbook of Theoretical and Computational Nanotechnology, American Scientific, Stevenson Ranch, CA, 2004 (Chapter 22).
[2] H. Lin, D.G. Truhlar, Theor. Chem. Acc. 117 (2007) 185.
[3] P. Sherwood, in: J. Grotendorst (Ed.), Modern Methods and Algorithms of Quantumchemistry, vol. 3, Princeton, 2000, p. 285.
[4] F.F. Abraham, R. Walkup, H. Gao, M. Duchaineau, T. de la Rubia, M. Seager, Proc. Natl. Acad. Sci. USA 99 (2002) 5777.
[5] N. Bernstein, J.R. Kermode, G. Csányi, Rep. Prog. Phys. 72 (2009) 026501.
[6] S. Ogata, R. Belkada, Comput. Mater. Sci. 30 (2004) 189–194.
[7] S. Ogata, Phys. Rev. B 72 (2005) 045348.
[8] N. Choly, G. Lu, W. E, E. Kaxiras, Phys. Rev. B 71 (2005) 094101.
[9] X. Zhang, G. Lu, Phys. Rev. B 76 (2007) 245111.
[10] X. Zhang, C.Y. Wang, G. Lu, Phys. Rev. B 78 (2008) 235119.
[11] M. Svensson, S. Humbel, R.D.J. Froese, T. Matsubara, S. Sieber, K. Morokuma, J. Phys. Chem. 100 (1996) 19357–19363.
[12] Y. Zhang, T.S. Lee, W. Yang, J. Chem. Phys. 110 (1999) 46.
[13] W.G. Han, M. Elstner, K.J. Jalkanen, T. Frauenhein, S. Suhai, Int. J. Quantum Chem. 78 (2000) 459–479.
[14] D. Das, K.P. Eurenius, E.M. Billings, P. Sherwood, D.C. Chatfield, M. Hodosceǩ, B.R. Brooksc, J. Chem. Phys. 117 (2002) 10534.
[15] H.P. Hratchian, P.V. Parandekar, K. Raghavachari, M.J. Frisch, T. Vreven, J. Chem. Phys. 128 (2008) 034107.
[16] T. Vreven, K. Morokuma, Ö. Farkas, H.B. Schlegel, M.J. Frisch, J. Comput. Chem. 24 (2003) 760–769.
[17] Y. Liu, G. Lu, Z. Chen, N. Kioussis, Model. Simul. Mater. Sci. Eng. 15 (2007) 275–284.
[18] M.J. Buehler, A.C.T. van Duin, W.A. Goddard III, Phys. Rev. Lett. 96 (2006) 095505.
[19] M.J. Buehler, H. Tang, A.C.T. van Duin, W.A. Goddard III, Phys. Rev. Lett. 99 (2007) 165502.
[20] I. Solt, P. Kulhánek, I. Simon, S. Winfield, M.C. Payne, G. Csányi, M. Fuxreiter, J. Phys. Chem. B 113 (2009) 5728–5735.
[21] N. Bernstein, D.W. Hess, Phys. Rev. Lett. 91 (2003) 025501.
[22] R.E. Cohen, M.J. Mehl, D.A. Papaconstantopoulos, Phys. Rev. B 50 (1994) 14694–14697.
[23] N. Bernstein, M.J. Mehl, D.A. Papaconstantopoulos, N.I. Papanicolaou, M.Z. Bazant, E. Kaxiras, Phys. Rev. B 62 (2000) 4477–4487.
[24] M.J. Mehl, D.A. Papaconstantopoulos, Phys. Rev. B 54 (1996) 4519–4530.
[25] W.A. Harrison, Electronic Structure and the Properties of Solids, Dover, New York, 1989.
[26] F.H. Stillinger, T.A. Weber, Phys. Rev. B 31 (1985) 5262.
[27] R.A. Johnson, Phys. Rev. B 37 (1988) 3924.
[28] M. Brede, K.J. Hsia, A.S. Argon, J. Appl. Phys. 70 (2) (1991) 758.
[29] J.Q. Broughton, F.F. Abraham, N. Bernstein, E. Kaxiras, Phys. Rev. B 60 (1999) 2391.
[30] G. Csányi, T. Albaret, M.C. Payne, A. DeVita, Phys. Rev. Lett. 93 (2004) 175503.
[31] J.A. Hauch, D. Holland, M.P. Marder, H.L. Swinney, Phys. Rev. Lett. 82 (1999) 3823.
[32] J.R. Kermode, T. Albaret, D. Sherman, N. Bernstein, P. Gumbsch, M.C. Payne, G. Csányi, A. DeVita, Nature 455 (2008) 1224–1227.
[33] T. Cramer, A. Wanner, P. Gumbsch, Phys. Rev. Lett. 85 (2000) 788C791.
[34] C.S. Becquart, D. Kim, J.A. Rifkin, P.C. Clapp, Mater. Sci. Eng. A 170 (1993) 87.
[35] W.C. O'Mara, R.B. Herring, L.P. Hunt, Handbook of Semiconductor Silicon Technology, Noyes Publications, NJ, 1990. p. 423.
[36] H.J.C. Berendsen, J.P.M. Postma, W.F. van Gunsteren, A. DiNola, J.R. Haak, J. Chem. Phys. 81 (1984) 3684–3690.
[37] G.C. Sih, H. Liebowitz, Fracture: An Advanced Treatise, vol. 2, Academic, New York, 1968 (Ch. Mathematical theories of brittle fracture, p. 68).
[38] G. Henkelman, B.P. Uberuaga, H. Jónsson, J. Chem. Phys. 113 (2000) 9901.
[39] G. Kresse, J. Hafner, Phys. Rev. B 49 (1994) 14251–14269.
[40] P.E. Blöchl, Phys. Rev. B 50 (1994) 17953–17979.
[41] J.P. Perdew, K. Burke, M. Ernzerhof, Phys. Rev. Lett. 77 (1996) 3865–3868.
[42] G. Henkelman, B.P. Uberuaga, H. Jónsson, J. Chem. Phys. 113 (2000) 9901.
[43] M.R. Sørensen, Y. Mishin, A.F. Voter, Phys. Rev. B 62 (2000) 2658.